






Article

Carbon Nanofibers Synthesized at Different Pressures for Detection of NO₂ at Room Temperature

Nikita I. Lapekin ¹, Pavel B. Kurmashov ¹, Tatyana V. Larina ², Yuri A. Chesalov ², Dmitry S. Kurdyumov ¹, Arina V. Ukhina ³, Evgene A. Maksimovskiy ⁴, Arcady V. Ishchenko ², Vitalii I. Sysoev ⁴ and Alexander G. Bannov ^{1,*}

¹ Department of Chemistry and Chemical Engineering, Novosibirsk State Technical University, 630073 Novosibirsk, Russia; lapekin21@mail.ru (N.I.L.); kurmashov@corp.nstu.ru (P.B.K.); kurdyumov@corp.nstu.ru (D.S.K.)

² Borekov Institute of Catalysis, Siberian Branch of Russian Academy of Sciences, 630090 Novosibirsk, Russia; larina@catalysis.ru (T.V.L.); chesalov@catalysis.ru (Y.A.C.); arcady.ishchenko@gmail.com (A.V.I.)

³ Institute of Solid State Chemistry and Mechanochemistry, Siberian Branch of Russian Academy of Sciences, 630128 Novosibirsk, Russia; auhina181@gmail.com

⁴ Institute of Inorganic Chemistry, Siberian Branch of Russian Academy of Sciences, 630090 Novosibirsk, Russia; eugene@niic.nsc.ru (E.A.M.); sysoev@niic.nsc.ru (V.I.S.)

* Correspondence: bannov.alexander@gmail.com

Abstract: In this paper, room-temperature chemiresistive gas sensors for NO₂ detection based on CVD-grown carbon nanofibers (CNFs) were investigated. Transmission electron microscopy, low-temperature nitrogen adsorption, and X-ray diffraction were used to investigate the carbon nanomaterials. CNFs were synthesized in a wide range of pressure (1–5 bar) by CO_x-free decomposition of methane over the Ni/Al₂O₃ catalyst. It was found that the increase in pressure during the synthesis of CNFs induced the later deactivation of the catalyst, and the yield of CNFs decreased when increasing pressure. Sensing properties were determined in a dynamic flow-through installation at NO₂ concentrations ranging from 1 to 400 ppm. Ammonia detection was tested for comparison in a range of 100–500 ppm. The obtained sensors based on CNFs synthesized at 1 bar showed high responses of 1.7%, 5.0%, and 10.0% to 1 ppm, 5 ppm, and 10 ppm NO₂ at 25 ± 2 °C, respectively. It was shown that the obtained non-modified carbon nanomaterials can be used successfully used for room temperature detection of nitrogen dioxide. It was found that the increase in relative humidity (RH) of air induced growth of response, and this effect was facilitated after reaching RH ~35% for CNFs synthesized at elevated pressures.

Keywords: gas sensors; carbon nanofibers; nitrogen dioxide; ammonia; adsorption; response



Citation: Lapekin, N.I.; Kurmashov, P.B.; Larina, T.V.; Chesalov, Y.A.; Kurdyumov, D.S.; Ukhina, A.V.; Maksimovskiy, E.A.; Ishchenko, A.V.; Sysoev, V.I.; Bannov, A.G. Carbon Nanofibers Synthesized at Different Pressures for Detection of NO₂ at Room Temperature. *Chemosensors* **2023**, *11*, 381. <https://doi.org/10.3390/chemosensors11070381>

Academic Editors: Nicole Jaffrezic-Renault and Marco Frasconi

Received: 30 March 2023

Revised: 29 June 2023

Accepted: 5 July 2023

Published: 7 July 2023



Copyright: © 2023 by the authors. Licensee MDPI, Basel, Switzerland. This article is an open access article distributed under the terms and conditions of the Creative Commons Attribution (CC BY) license (<https://creativecommons.org/licenses/by/4.0/>).

1. Introduction

One of the most harmful air pollutants, nitrogen dioxide (NO₂), is well known to be harmful to human health. For instance, it may result in lung cancer, asthma, and respiratory infections [1–4]. Nitrogen dioxide reacts with water on moisture-exposed tissues forming nitric acid, which is highly corrosive and dangerous. It can pass through the upper respiratory tract with little effect and then react with water in the lungs, causing severe tissue damage. Toxicity depends on both the concentration of the gas and the duration of exposure, but short-term exposure to high concentrations tends to be more harmful than longer-term exposure to low concentrations [5]. Thus, the monitoring of NO₂ in the air is a priority for occupational and life safety [6].

One of the reliable ways to determine the nitrogen dioxide concentration is using chemiresistive gas sensors, the resistance of which changes with NO₂ content in air [7]. Today, commercial sensors based on semiconductors are widely used, but the operation of such sensors is associated with many problems, for example, their high power consumption, which is due to the need to heat the sensing layer above 250–300 °C [8–10]. The

drawbacks of traditional semiconductor-based gas sensors can be solved by the application of nanomaterials as active layers for the sensors making it possible to operate at room temperature [11]. Surface acoustic wave sensors are also used for NO₂ detection [12,13], but the chemiresistive sensors are considerably cheaper.

There are a lot of nanomaterials and composites applied for NO₂ detection at room temperature, such as ZnO [14,15], CuO-ZnO [16], Co₃O₄-ZnO [17], SnO₂-NiO [18], In₂O₃@GO [19], SnO [20], gallium oxyselenides [21], transition metal carbides/nitrides and their composites (MXenes) (such as Mo₂TiC₂T_x/MoS₂ [22], TiO₂/Ti₃C₂ [23], Ti₃C₂T_x/TiO₂/rGO [24]), etc. Special attention is paid to carbon nanomaterials because of the great variety of modifications [25–28]. In particular, carbon nanomaterials, such as single-walled carbon nanotubes (SWCNTs) [29,30], multiwalled carbon nanotubes (MWCNTs) [31,32], double-walled carbon nanotubes (DWCNTs) [33], as well as carbon nanofibers (CNFs) [34–37] are already investigated for NO₂ detection.

Carbon nanofibers, being a by-product of catalytic decomposition of methane (or other hydrocarbons) for hydrogen synthesis, are of greater interest for applications in sensing due to their relatively low cost, higher yield compared to SWCNTs and MWCNTs, almost no need for purification [34], and easier process of production [38,39]. This material can be produced both in the form of powder and granules, which is determined by the content of the active components (nanoparticles of transition metals) of the catalyst and type of reactor (fluidized bed, vibrofluidized bed, and fixed bed) [40,41]. At the same time, there is no data reported on the application of CVD-grown CNFs, synthesized at pressures above 1 bar, for gas sensing. There is only one paper devoted to the creation of NO₂ gas sensors based on granulated carbon nanofibers synthesized at atmospheric pressure [34]. For the synthesis of CNFs, it is important to control the synthesis parameters (e.g., temperature and pressure inside the reactor) since changes in parameters will make it possible to obtain carbon material with different disorder degree, texture characteristics (specific surface area, pore size, nanofiber length, etc.). All these characteristics will reflect on the sensing behavior. Such studies have not been carried out before. The impact of pressure on the growth of CNFs and the sensing behavior of materials is a novel and relatively cheap approach to modify the characteristics of sensors. Usually, the sensor response can be modified via chemical modification [42,43] of carbon nanomaterials, but the control of pressure needs no additional chemical reagents and does not lead to a decrease in the yield of material compared to chemical treatment.

This work is the first one devoted to the creation of room-temperature nitrogen dioxide sensors based on CNFs synthesized at different pressures (1–5 bar) over 90%Ni/Al₂O₃ catalyst using the CVD technique. The sensing behavior of CNFs for the detection of nitrogen dioxide in a range of 1–400 ppm NO₂ was investigated. Ammonia detection at room temperature was also studied for comparison. Thermodynamic characteristics of the NO₂ adsorption process were also calculated in order to predict the adsorption mechanism. The distinctive feature of this paper is the use and investigation of three different CNF materials synthesized at various pressures. This technique can be considered as a novel way for modification of adsorption behavior of sensing material by means of increasing the pressure of growth of the CNFs.

2. Materials and Methods

2.1. Synthesis of CNFs and Characterization Techniques

Carbon nanofibers were synthesized by catalytic decomposition of methane in the flow through installation BTRS-Jr (Autoclave Engineers, Houston, TX, USA) at pressures above 1 bar. The catalyst containing 90% Ni/10% Al₂O₃ was used for the growth of CNFs at the temperature of 535 °C and pressure ranges from 1 to 5 bar. The technique of preparation of Ni/Al₂O₃ catalyst was described in [44] in detail. Briefly, the catalyst was obtained by solution combustion technique. The authors dissolved the nitrates (Ni(NO₃)₂·6H₂O and Al(NO₃)₃·9H₂O) in 100 mL of deionized water and added the hexamethylenetetramine (HTMA) as fuel with a fuel excess coefficient of 1 ($\varphi = 1$). The solution was heated to

100 °C for dehydration, and further ignition of the mixture using the gas burner with the subsequent formation of catalytic nanoparticles was carried out. The catalyst was placed in a vertical reactor of BTRS-Jr (Autoclave Engineers, USA) installation, and CNFs were grown at 1 bar (the sample was named “CNFs-1”), 3 bar (“CNFs-3” sample) and 5 bar (“CNFs-5” sample) at 535 °C.

The following methods were used for the characterization of synthesized carbon nanomaterials.

Transmission electron microscopy (TEM) was used to estimate the morphological features of the obtained CNFs using JEM-2200FS (Jeol, Tokyo, Japan) with an accelerating voltage of 200 kV and lattice resolution of 1 Å. For TEM investigation, the samples were preliminary ultrasonicated in ethanol solution and deposited onto a carbon sheet supported on a copper grid.

Low-temperature nitrogen adsorption was used for the characterization of the porosity of CNFs using Quantachrome NOVA 1000e installation. The samples were preliminarily degassed in a vacuum at 300 °C at 6 h in order to remove the adsorbed compounds. Isotherms of adsorption and desorption were taken at a 77 K of temperature and in the range of relative pressure of nitrogen of 0.005–0.995. The Brunauer–Emmett–Teller (BET) method was used to determine the specific surface area.

X-ray diffraction (XRD) was used to determine the crystallite size of CNFs and traces of catalyst using a D8 Advance diffractometer (Bruker, Mannheim, Germany). The crystallite size of CNFs, Ni, was determined using Rietveld analysis in TOPAS 4.2 software (Bruker AXS).

The features of disorder degree of the CNFs were determined by Raman spectroscopy on a T64000 (Horiba Jobin Yvon, Longjumeau, France). The 514 nm Ar⁺ laser was used as the Raman excitation source. The power of radiation reaching the sample was 0.2 mW. The degree of disorderliness of the carbon materials (degree of defectiveness) was estimated from the ratio of the intensities of D and G peaks.

2.2. Sensors Preparation Technique

Figure 1 shows the flowchart of the technique used for the sensor preparation. The active layer of the gas sensor was obtained by drop-casting of the CNF sample in the thick dielectric substrate. The dielectric substrate made of several layers of glass fabric soaked with epoxy resin (textolite) with thin copper contacts on the edges of one side was mechanically polished with abrasive paper down to 600 grids and cleaned with ethanol solution. The suspension of CNFs (particles with a size below 100 µm were used) was prepared by their dispersion in ethanol solution in the ultrasonic bath (UZV-3/200, RELTEK, Russia) at the power 85 W for 20 min (frequency was 22 kHz). CNFs (0.03 g) were dispersed in 5 mL of ethanol. During droplet application on the heated (80 °C) substrate, the film (5 × 5 mm) was formed, partially covering the copper contacts.

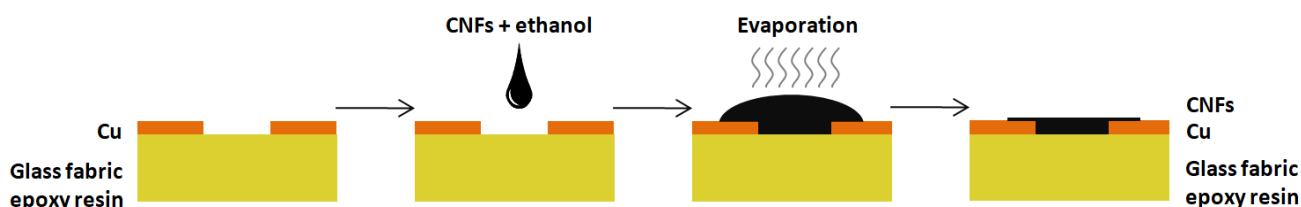


Figure 1. Sensors preparation technique.

2.3. Gas Sensing Procedure

The setup for the detection of the hazardous gas in the air is shown in Figure 2.

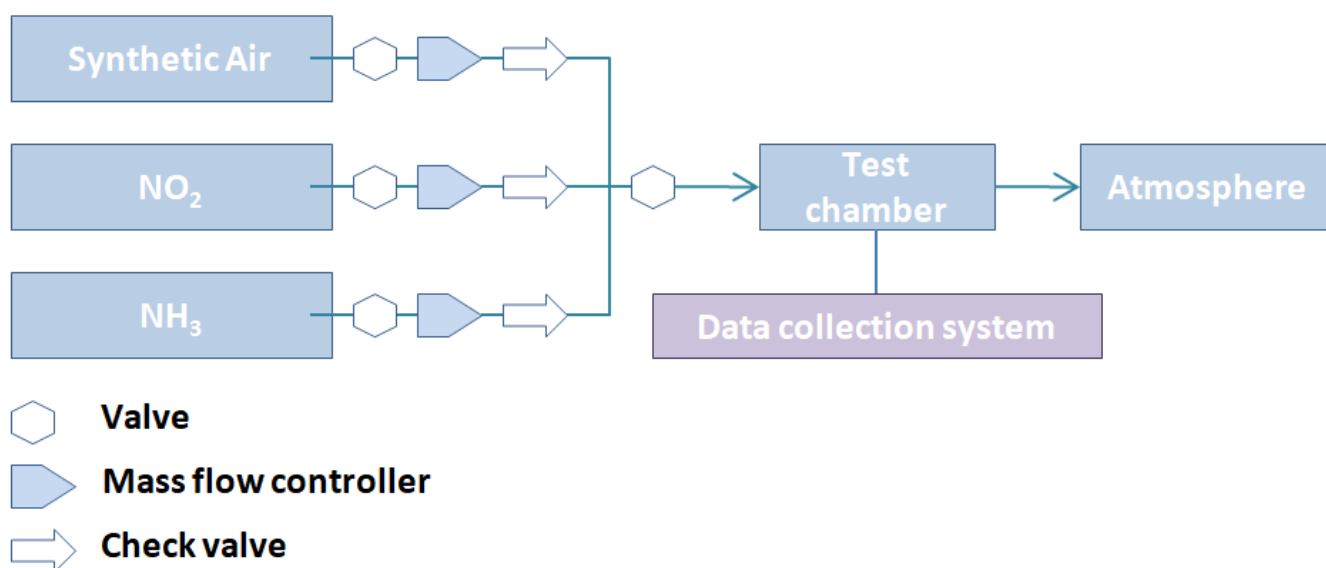


Figure 2. Setup for testing of sensors in a dynamic regime at room temperature.

The setup included flows of analytes and carrier gas (synthetic air containing 21 vol.% O₂, 79 vol.% N₂). The mixture of nitrogen dioxide in air (i.e., 500 ppm NO₂ in air), a mixture of ammonia and air (i.e., 5000 ppm NH₃ in air) were used as model gases for the investigation of CNF-based sensors.

The total flow rate fed into the test chamber was 100 mL/min. The concentration of the analyte in the system was achieved by adjusting the ratio of gas flows from the cylinders using mass flow controllers.

The measurement technique included the following steps. First, the system was purged with a carrier gas (synthetic air) for 10 min with a flow rate of 100 mL/min in order to clean the system from the residual analyte molecules. After that, the sensor was placed in the cell with two copper electrodes and heated inside to 70 °C and kept for 10 min in a 100 mL/min flowing of synthetic gas to carry out the desorption of compounds from the surface of the sensor and decrease the level of relative humidity (RH) inside the cell up to 1 ± 0.1%. The testing of sensors was performed in dry air (1%) and at higher relative humidity using an additional line with wet synthetic air fed into the chamber.

Then, the system was cooled down for 20 min at a flow rate of 1000 mL/min to decrease the temperature inside the cell to room temperature (25 ± 2 °C). The next step consisted of measuring the baseline of 60 min in synthetic air (100 mL/min) followed by 10 min cycles of analyte/air mixture fed alternated by 10-min-cycles of synthetic air.

The changes in resistance of the sensors were recorded using a Keithley 2401 source meter (Keithley Instruments, Inc., Cleveland, OH, USA) at a voltage bias of 0.1 V. Data acquisition was performed by KickStart software (Tektronix, Inc., Beaverton, OR, USA).

To evaluate the behavior of the sensors to NO₂ and NH₃ gases, the relative response of the sensors was calculated as the ratio between the change in sensor resistance (ΔR) during the contact with the analyte and the initial resistance (R_0) in air, using the following equation:

$$\frac{\Delta R}{R_0} = \frac{R - R_0}{R_0} \cdot 100\%, \quad (1)$$

where R is the electrical resistance of the sensor when exposed to analyte, Ω ; R_0 is the initial electrical resistance of the sensor when exposed to carrier gas (air), Ω .

3. Results

3.1. Characterization of CNFs

TEM micrographs of CNFs (Figure 3) showed the formation of cup-stacked cone (or so-called fishbone structure [45,46]) nanofibers with a diameter of 40–150 nm. Since the catalyst

composition was the same for all samples, there is no difference in the structure of CNFs, and it is typical for materials synthesized over Ni-containing catalysts [47]. The increase in pressure induced the later deactivation of the catalyst; however, the yield of CNFs decreased when increasing pressure. The formation of catalyst by solution combustion also induced the growth of nanofibers with smaller diameters (20–30 nm). The average diameter of CNFs was 44.9 ± 5.5 nm (CNFs-1), 78.5 ± 6.4 nm (CNFs-5), and 61.46 ± 3.4 nm. The data show that the lower diameter of CNFs was formed at 1 atm pressure of methane catalytic decomposition.

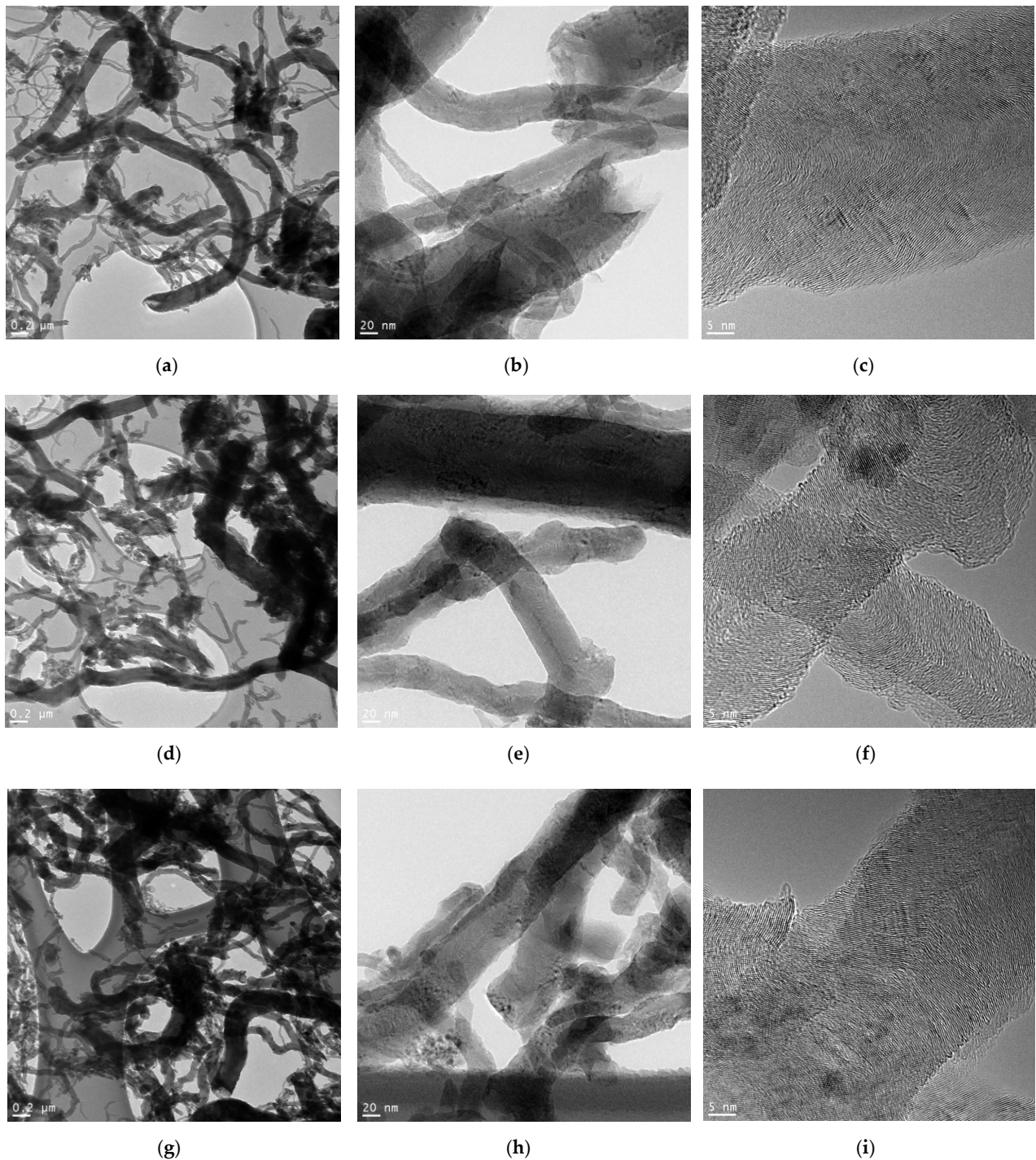


Figure 3. TEM-micrographs of CNFs-1 (a–c); CNFs-3 (d–f); CNFs-5 (g–i).

One considering the yield of CNFs, it is clearly seen that this value decreased when increasing pressure, e.g., 268.3 g/g_{cat} (CNFs-1), 12.0 g/g_{cat} (CNFs-3) and 10.1 g/g_{cat} (CNFs-5) (Table 1). According to low-temperature nitrogen adsorption, all CNF samples consisted of mesopores fully without the contribution of other types of pores. The average pore size increases when increasing pressure from 10.3 nm to 12.4 nm. The total pore volume grows from 0.28 to 0.40 cm³/g. CNFs-1 synthesized at 1 atm showed 108 m²/g specific surface area, and further increase in pressure led to a decrease of the latter to 101 m²/g with the subsequent growth at 5 atm to 129 m²/g. This is also surprising and indicates the complex mechanism of the formation of carbon nanofibers at a pressure higher than 1 atm. According to data on the yield, which dropped when increasing pressure from 268.3 g/g_{cat} to 10.1 g/g_{cat}, the specific surface area decreases at 3 atm and then begins to increase to grow to 21 m²/g compared to the CNFs-1 sample.

Table 1. Characterization of obtained CNFs.

Sample	Specific Flow Rate of Methane, L/(h·g _{cat})	Pressure, atm	Yield of CNFs, g/g _{cat}	Specific Surface Area, m ² /g	Average Pore Size, nm	Total Pore Volume, cm ³ /g
CNFs-1	90.0	1	268.3	108	10.3	0.28
CNFs-3	90.0	3	12.0	101	10.7	0.27
CNFs-5	90.0	5	10.1	129	12.4	0.40

XRD patterns of CNFs are presented in Figure 4. The samples were almost fully represented by the phase of graphite (*P6₃/mmc* space group) with the strong (002) reflection typical for a majority of carbon nanomaterials [48,49]. All samples contained nickel phase additionally (*Fm3m* space group), since the nickel oxide is reduced by hydrogen (formed as a result of methane decomposition), and the growth of nanofibers begins on nickel catalytic nanoparticles. The size of Ni crystallites is hard to be calculated because of its low concentration and high error of the calculation. Since the growth of CNFs was carried over the Ni/Al₂O₃ catalyst, the content of the latter is low (below the detection limit of the technique), and there are no reflections related to the alumina phase in the XRD patterns.

Raman spectra of CNFs are shown in Figure 5.

The bands about 1595 and 1355 cm⁻¹ were observed in the spectra of all samples in the spectral region of the first order (1200–1600 cm⁻¹). The band around 1590 cm⁻¹ (G (Graphite) band) corresponds to the vibrational mode with the E_{2g} symmetry of the ideal graphite lattice. The band around 1350 cm⁻¹ (D or Defective Band) is absent in the spectra of single-crystal graphite and HOPG (highly oriented polycrystalline graphite). The D band corresponds to the vibrational mode with the A_{1g} lattice symmetry of graphite. The appearance of the defective band in the spectra of carbon materials is associated with the disordered structure. The increase in its intensity relative to the intensity of the G band is associated with an increase in the number of defects in the graphite structure [50]. The D/G ratio of intensities is given in Table 2.

It is shown that the defectiveness of CNFs changes when increasing pressure, and initially, it begins to decrease when pressure exceeds 1 bar. Then, it grows slightly during the pressure rising from 3 to 5 bar. It can be explained by complex behavior of CNF growth under pressure above 1 bar, since each increase in pressure prolongs the lifetime of catalyst. The increase in pressure brings no changes in the type of defects in CNFs, but it has an effect on diameter of CNFs and length consequently. The increase in pressure led to decrease in yield of CNFs as a result of decrease in conversion of methane. Probably, there is an impact of pressure on the rate of carbon formation on the catalyst, which is high enough for 1 atm and begins to decrease when increasing pressure. The increase in this rate of carbon formation at 1 atm leads to formation of strongly curved nanofibers which is apparently shown by Raman spectroscopy and the highest I(D)/I(G) ratio. The diameter of nanofibers in CNFs-1 was the lowest one (44.9 ± 5.5 nm) compared to two other samples, and this factor along with high growth rate induces higher curvature of CNFs and defectiveness.

The CNFs with higher curvature degree possessed higher concentration of defects, since these regions are under strain. Such an effect was discussed in [51] using single-walled carbon nanotubes as the model object.

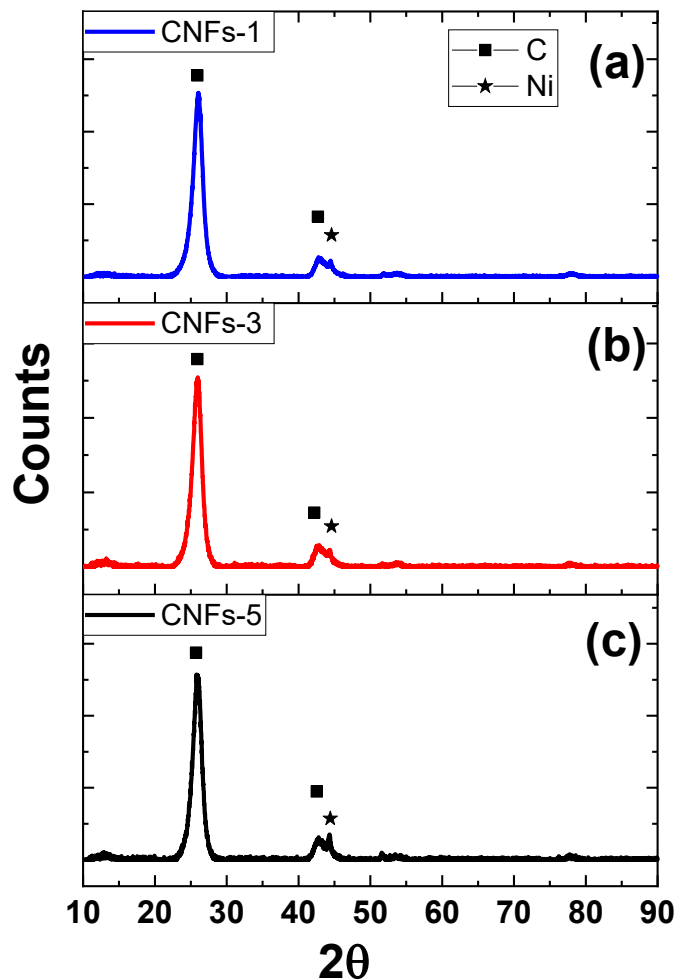


Figure 4. XRD patterns of CNFs-1 (a); CNFs-3 (b); CNFs-5 (c) (Cu $K\alpha$ radiation).

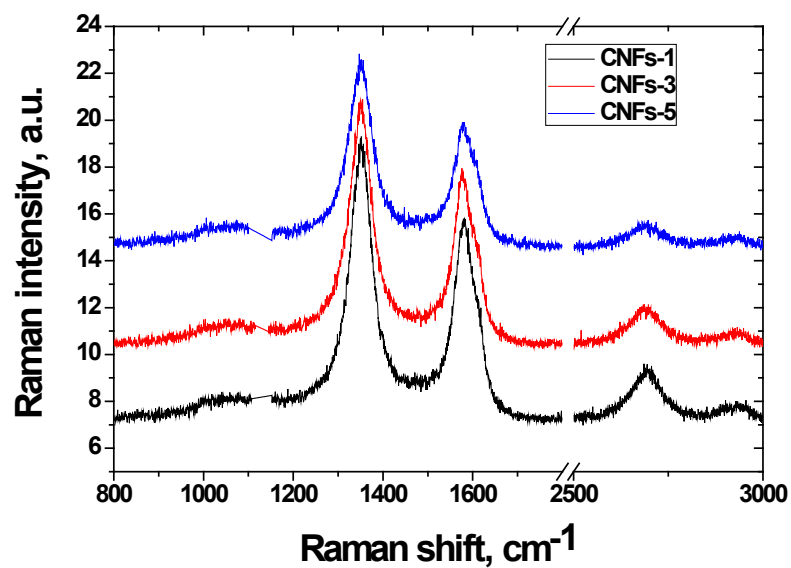


Figure 5. Raman spectra of CNFs ($\lambda = 514$ nm).

Table 2. I(D)/I(G) ratio of CNFs.

Sample	I(D)/I(G)
CNFs-1	2.00
CNFs-3	1.69
CNFs-5	1.84

3.2. Gas Sensing Properties

Figure 6 shows the response of sensors based on CNFs. They possess a high response towards NO_2 at concentrations above 100 ppm.

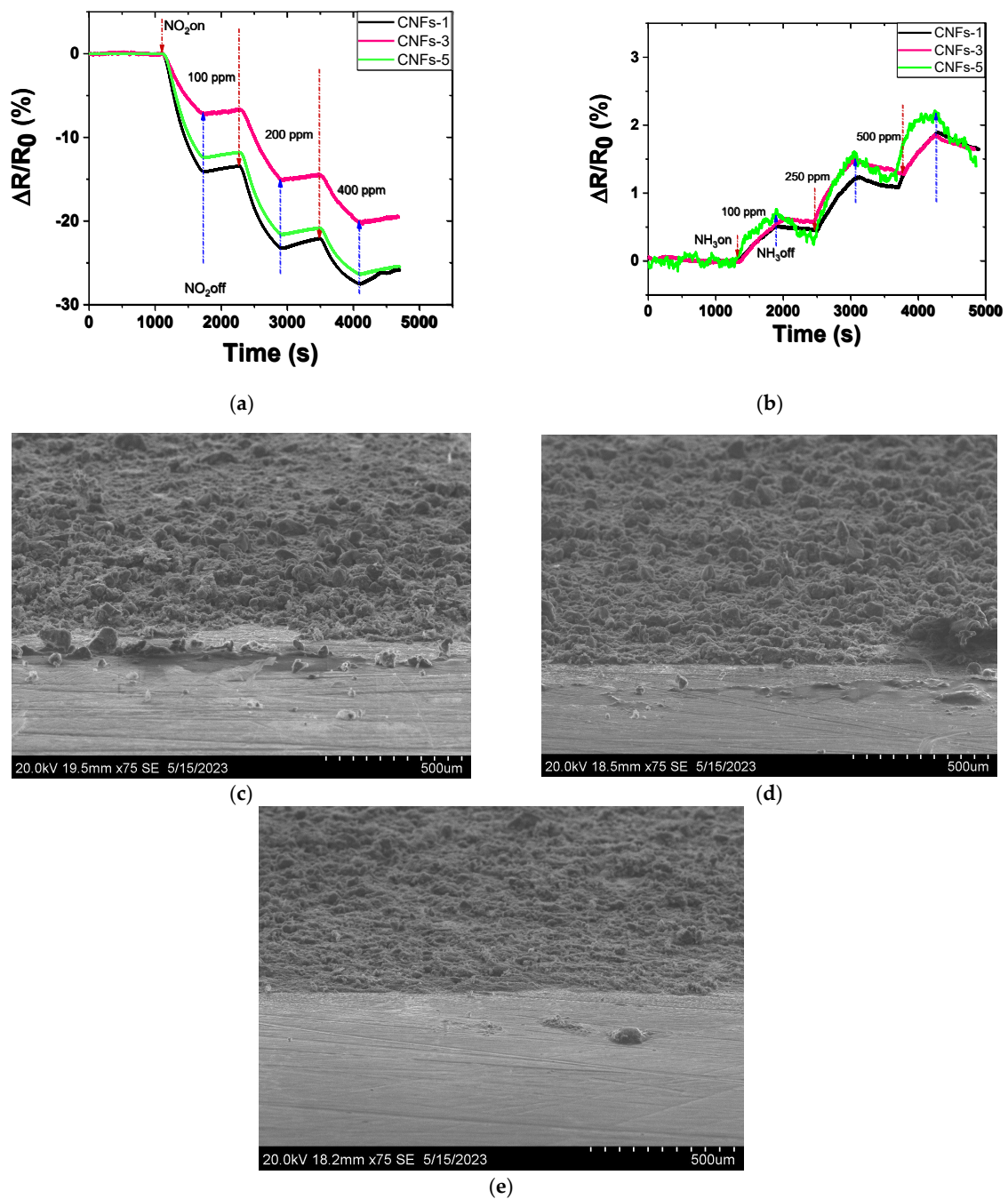


Figure 6. Response of obtained CNFs to 100–400 ppm of NO_2 (a) and 100–500 ppm of NH_3 (b) at room temperature (25 ± 2 °C, RH = 1%); SEM images of CNFs on the substrate: CNFs-1 (c), CNFs-3 (d), CNFs-5 (e).

The response to NO₂ grows stronger until reaching 250 ppm, after which it had a smaller change when increasing concentration. This effect was also found in [33,52,53] and is typical for different types of carbon nanomaterials. Usually, the higher concentration of analyte brings the system closer to the filling of adsorption sites, and further change in concentration makes a small effect on sensor response. The resistance change vs. concentration of nitrogen dioxide can be considered as non-linear. For example, response curve of CNFs-1 might be fitted with $y = a + b \cdot x^c$ function with $a = 211.438$, $b = -221.99$, $c = 0.01918$ ($R^2 = 0.972$). The power c in the same type of equation for CNFs-3 and CNFs-5 was 0.24752 ($R^2 = 0.975$, $a = 9.496$, $b = -8.287$) and 0.28614 ($R^2 = 0.978$, $a = 5.098$, $b = -4.578$), respectively, showing that the pressure increase making the response behavior relatively closer to power function relation.

The testing of gas sensors for NH₃ detection was also carried out for comparison since this is a different type of gas in terms of its interaction with the surface of carbon nanomaterials [54]. The maximum response of CNFs to NH₃ was low enough and less than 3%, which is typical for non-functionalized carbon nanomaterials [55,56]. The higher concentrations of ammonia were taken because of the low sensitivity of CNFs to the latter. It was impossible to measure resistance without high noise and the error below 50–100 ppm NH₃ in air. So it can be indirectly concluded that the obtained sensors are selective to adsorb the nitrogen dioxide compared to ammonia.

It is well known that mostly carbon nanomaterials act as p-type semiconductor materials due to the defects acting as charge transfer centers [57]. The negative slope of the NO₂ resistance vs. concentration relation is associated with a decrease in the resistance of the CNFs during its adsorption. This is due to the fact that the adsorption of electron acceptor compound as nitrogen oxide on the surface of sample causes transfer of electrons from the nanofibers, which increases the concentration of holes and increases the conductivity. Conversely, the increase in sensor resistance during ammonia adsorption by CNFs is caused by the electron donating nature of ammonia, adsorption of which reduces the concentration of charge carriers (holes, namely) leading to a decrease in conductivity. At the same time the investigated CNF samples contain not so much centers of ammonia interacting with surface compared to other carbon materials (e.g., graphene [58], graphene oxide [59], graphite oxide [60], functionalized carbon nanotubes [61] etc.) and this explains their low response to NH₃.

Further, the impact of pressure on the sensing behavior of CVD-grown CNFs will be discussed. Increasing the pressure in the catalytic decomposition of methane promoted the formation of CNFs with different specific surface areas and disorder degrees, resulting in reduced response to NO₂. SEM images of CNFs on the substrate were shown in Figure 6c–e indicating the coverage of the surface of textolite with aggregated carbon nanofibers. SEM images with higher magnification are presented in Supplementary Materials. The response of CNF-based films is given in Table 3.

Table 3. Response to nitrogen dioxide of the sensors based on CNFs as an active layer at room temperature and RH = 1%.

Sample	Analyte	$\Delta R/R_0$, %			R_{25° *, Ω
		100 ppm	200 ppm	400 ppm	
CNFs-1	NO ₂	−14.1	−23.2	−27.5	603
CNFs-3	NO ₂	−7.3	−15.2	−20.3	830
CNFs-5	NO ₂	−12.4	−21.6	−26.3	447

* R_{25° —Resistance of active layer in air at room temperature.

The sensor CNFs-1 showed the best response to the analytes due to the highest disorder degree, estimated using Raman spectroscopy ($I(D)/I(G) = 2.0$). The response to 100–400 ppm NO₂ ranged from −14.1 to −27.5% and 0.5–1.9% to NH₃. As can be seen, the sensors based on CNFs taken without any treatment possess a better response to

NO_2 compared to NH_3 (Table 4). Since the content of surface functional groups has high importance for NH_3 detection in carbon nanomaterials [52,62], the CNF samples showed a relatively low $\Delta R/R_0$, typical for non-functionalized carbon nanomaterials [63,64].

Table 4. Response to ammonia of the sensors based on CNFs at room temperature and RH = 1%.

Sample	Analyte	$\Delta R/R_0$, %		
		100 ppm	250 ppm	500 ppm
CNFs-1	NH_3	0.5	1.2	1.9
CNFs-3	NH_3	0.6	1.5	1.9
CNFs-5	NH_3	0.8	1.6	2.1

Because of the high response to 100 ppm NO_2 , it can be indirectly suggested that the sensors are also capable of detecting lower concentrations of NO_2 . To confirm this, the obtained sensors were tested in a lower range of 1–50 ppm NO_2 (Figure 7).

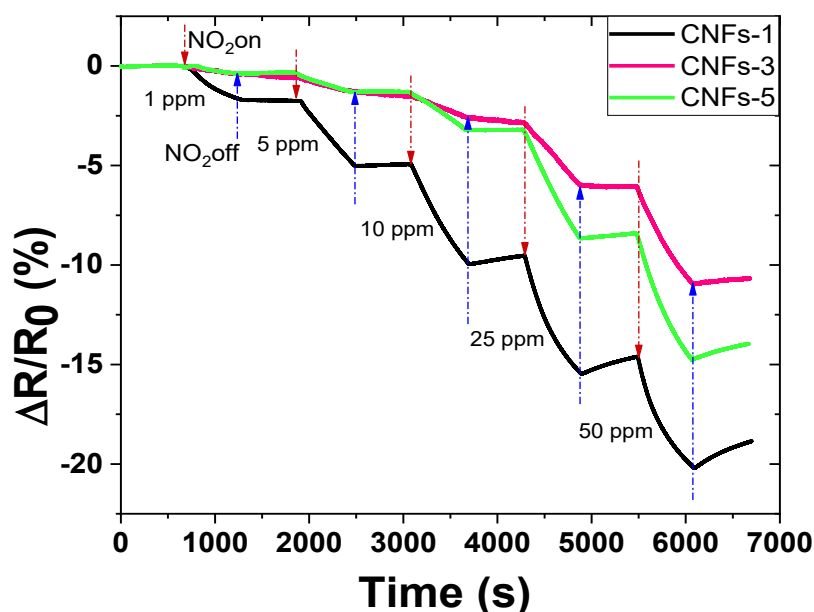


Figure 7. Response of obtained CNFs to 1–50 ppm of NO_2 and at room temperature ($25 \pm 2^\circ\text{C}$) and RH = 1%.

The obtained sensors demonstrated a good response towards 1–50 ppm of NO_2 (Table 5), but the data had no correlation with data on the specific surface area of obtained CNFs. The increase in the surface area did not lead to an increase in response. On the contrary, the highest response was observed for the CNFs-1, obtained at 1 atm. In spite of the sensors are shown recovery during the carrier gas feeding, purging after 1 ppm of NO_2 did not lead to recovery of resistance. This is presumably due to the thermodynamic stability of the system in which the carrier gas was fed, and the dimensions of the testing chamber do not lead to a shift of the equilibrium to a desorption state fully.

3.3. Adsorption Isotherms

The response of CNF-based sensors depending on NO_2 concentration (Figure S2 in Supplementary Materials) was treated with different adsorption isotherms used to understand the behavior of sensing material under contact with nitrogen oxide. Langmuir [30,65] and Freundlich [66,67] isotherms were used to fit the experimental data; the explanation of the equations was given in Supplementary Materials. The fitting data of curves of response using different isotherm theories are shown in Table 6.

Table 5. Response of sensors based on CNFs at room temperature and RH = 1%.

Sample	Analyte	$\Delta R/R_0$, %				
		1 ppm	5 ppm	10 ppm	25 ppm	50 ppm
CNFs-1	NO ₂	−1.7	−5.0	−10.0	−15.5	−20.2
CNFs-3		−0.4	−1.3	−2.6	−6.0	−11.0
CNFs-5		−0.4	−1.3	−3.2	−8.7	−14.8

Table 6. Summary of isotherm fitting parameters for obtained CNFs.

Isotherm	CNFs-1				CNFs-3				CNFs-5			
	R ²	Q _m , %	K, Pa ^{−1}	n	R ²	Q _m , %	K, Pa ^{−1}	n	R ²	Q _m , %	K, Pa ^{−1}	n
Freundlich	0.911	n/a	10.01	0.29	0.961	n/a	3.95	0.45	0.949	n/a	5.47	0.44
Langmuir	0.988	27.34	0.53	1.00	0.983	22.38	0.15	1	0.991	29.593	0.17	1
Modified Langmuir	0.989	27.53	0.53	0.98	0.983	22.93	0.15	0.96	0.993	27.19	0.15	1.20

Fitting parameters shown in Table 6 show that experimental data can be treated with the best fit using modified Langmuir isotherm [68] ($R^2 = 0.989–0.993$) and classical linear Langmuir isotherm [69]. The results of the calculation of adsorption energy (Table 7; calculation equations were presented in Supplementary Materials) showed the physical behavior of adsorption of NO₂ by all CNFs' samples since the enthalpy of adsorption was below 1 eV [70].

Table 7. Enthalpy of NO₂ adsorption on films of CNFs at room temperature.

Isotherm	CNFs-1	CNFs-3	CNFs-5
	ΔH , eV	ΔH , eV	ΔH , eV
Freundlich	0.118	0.071	0.087
Langmuir	0.033	0.096	0.092
Modified Langmuir	0.033	0.096	0.096

The enthalpy of adsorption increased for the set from CNFs-1 to CNFs-5 samples. Previously, we have found that the granulated carbon nanofiber material, synthesized over Ni/Al₂O₃ catalyst obtained by coprecipitation technique and synthesized at 1 atm and 550 °C, has also shown the physical nature of NO₂ adsorption [34]. However, the enthalpy of adsorption in [34] was 2–5 times of magnitude higher compared to CNFs studied in this paper. Apparently, this is caused by the higher disorder degree of CNFs investigated in this paper (according to Raman spectroscopy I(D)/I(G) was 1.69–2.0 compared to 0.98 for granulated CNF in [34]). This is given at an assumption that the surface area of CNFs studied and granulated CNFs reported in [34] seems to be similar (101–129 m²/g compared to 110 m²/g for granulated CNF studied in [34]). The Langmuir constant K in the modified Langmuir equation was 0.15–0.53, and it was considerably higher than reported in [34] (K = 0.03), showing the stronger interaction of the surface of CNFs with nitrogen dioxide molecules.

A comparison of response data of the CNF-based sensors for NO₂ detection to literature data is shown in Table 8. Considering that the obtained materials were non-modified and used in pristine form, our CNFs are effective and prospective for NO₂ detection at room temperature.

Table 8. Performance of NO₂ sensor based on CNFs and a comparison with published data.

Active Layer of Sensor	NO ₂ Concentration, ppm	$\Delta R/R_0$, %	Temperature, °C	Reference
WS ₂ /CNFs	10.0	2.11	25 (RT)	[71]
CNFs	10.0	1.63	25 (RT)	[72]
CNFs	1.0	2.00	25 (RT)	[35]
CNFs	10.0	3.00	25 (RT)	[73]
TiO ₂ -carbon black	10.0	2.50	50	[73]
CNFs (CNFs-1 sample)	10.0	10.00	25 (RT)	This work

3.4. Humidity

The effect of relative humidity on the sensing behavior of CNFs is an important factor to consider in the design and optimization of gas sensors based on these materials. The effect of relative humidity on the sensor response was studied (Figure 8).

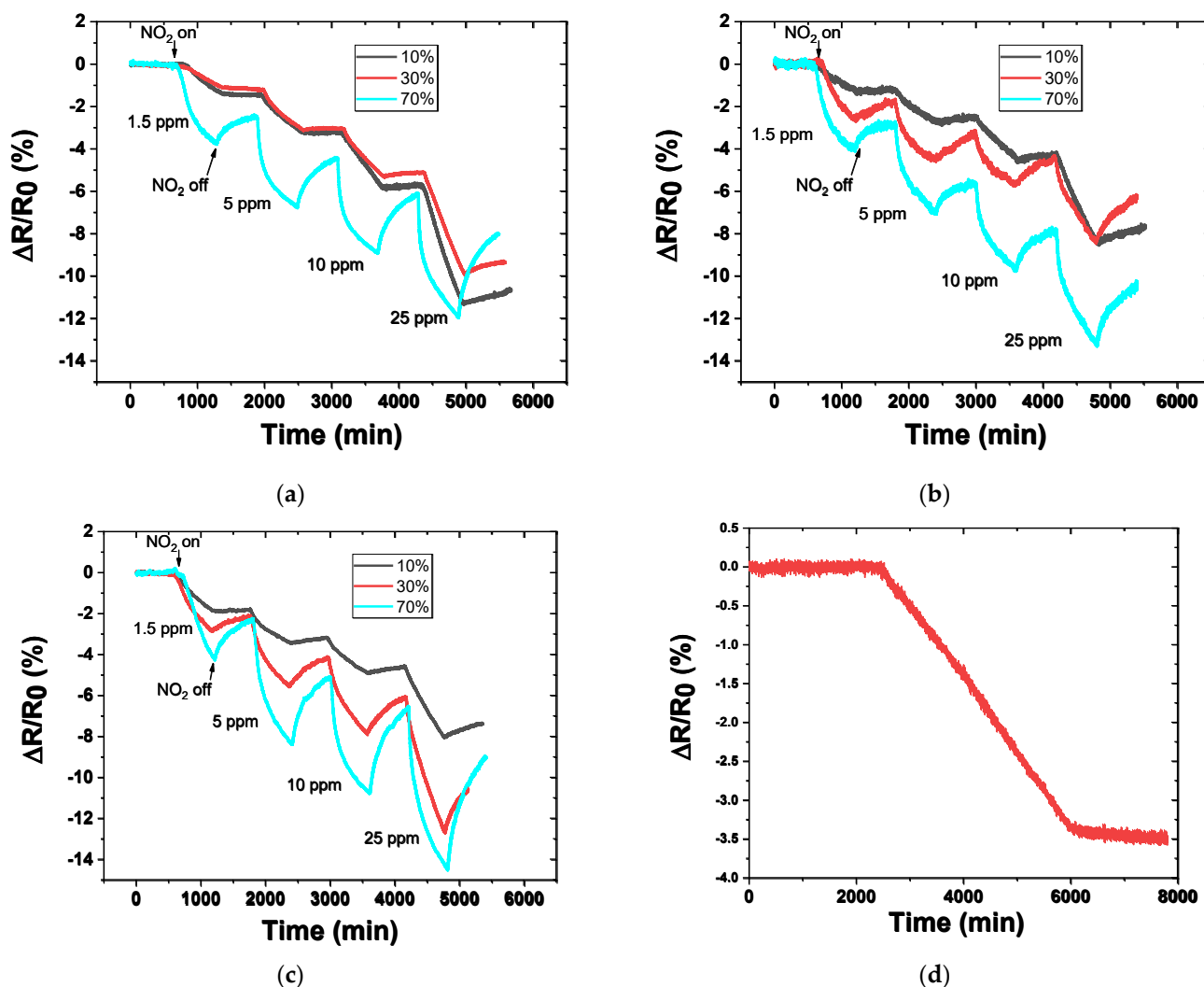


Figure 8. Effect of relative humidity on the NO₂ response at room temperature: CNFs-1 (a); CNFs-3 (b); CNFs-5 (c); long-term stability sensor curve at 1.5 ppm NO₂ at 1% RH; An example of the long-term stability curve of the CNFs-1 sample in dry air (RH = 1%) is shown in (d).

It was found that the increase in RH induced a growth of response. There is almost no effect of humidity at RH = 10–35%. After reaching an RH of ~35%, the response begins to increase with increasing RH (−3.6% at 1.5 ppm NO₂ and RH = 70% compared to −1.3% at RH = 30% at the same concentration of nitrogen dioxide). This effect confirms the data

reported in [74,75]. The increase in humidity leads to an increase in the concentration of charge carriers caused by the donation of protons (H^+ or H_3O^+) from water in air. The Grotthuss-type mechanism is usually used to explain the donation of protons in humidity-enhanced sensors [76,77]. The growth of RH makes the moving of protons better, including an enhancement of sensing performance [77]. According to the data obtained, the effect of humidity becomes higher with an increase in the pressure of CNF synthesis. The humidity-enhanced response of the CNFs-5 sample is probably caused by the higher specific surface area and average pore size of these CNFs. It is interesting that the most defective CNFs-1 sample showed a less humidity-dependent response, indicating the insignificant role of defectiveness in the transport of protons and their absorption by the sample. This effect could be attributed to the saturation of the surface sites of the CNFs with water molecules that leads to a higher concentration of charge carriers and a more efficient sensing response. Moreover, it is clearly seen in Figure 8 that the degree of recovery enhances with increasing RH. For example, at 1.5 ppm, NO_2 CNFs-5 sample shows 3%, 16%, and 44% of recovery at RH 10%, 30%, and 70%, respectively.

The humidity tests showed that even if CNFs were synthesized at a pressure higher than 1 atm, these samples showed a huge humidity-enhanced response. This feature of materials could be a benefit for operating sensors in wet conditions or other gas mixtures with high humidity level.

3.5. Response Time

The response time of sensors (time until reaching 90% of maximum sensor response at a certain concentration) was analyzed for three main concentrations within a range of 1–100 ppm NO_2 (Table 9).

Table 9. Response time of sensors at various concentrations (RH = 1%, room temperature).

Sample	Response Time, s (at Various NO_2 Concentrations)		
	1 ppm	10 ppm	50 ppm
CNFs-1	504	525	477
CNFs-3	465	517	507
CNFs-5	465	520	480

The response time was slightly higher than that of sensors based on carbon nanomaterials or graphite-related materials [78] and lower compared to various semiconductor-based sensors [79,80]. The difference in response time is caused not only by the type of sensing material but also by the design of the testing chamber, the flow rate of air, and the type of testing setup. The time of exposure at which the measurement is carried out and the concentration also contributes to the determination of response time. The effect of these factors on response time can be observed in the long-term stability test. An example of the long-term stability curve of the CNFs-1 sample in dry air (RH = 1%) is shown in Figure 8d. As can be seen, the low concentration of analyte (i.e., NO_2) leads to the absence of saturation of the sensor.

Interestingly an increase in relative humidity made the response faster (as shown by the shape of the curve in Figure 8). For example, the response time of the CNFs-1 sample at 10 ppm and RH = 70% was 395 s compared to 525 s (RH = 1%).

It is worth noting that there is no direct correlation between the response time of the sample. The second important characteristic is recovery time, but it is not possible to precisely analyze this value since the recovery was incomplete and the point of 90% of recovery shifts for each concentration.

Overall, the response time of the CNFs-based sensor is comparable to that of other types of sensors and can be optimized by adjusting the testing conditions and the design of the sensing chamber. The long-term stability of the sensor is also affected by these factors, as well as the concentration of the analyte and the type of sensing material used. Further

research is needed to fully understand the mechanisms behind the response time and stability of CNF-based sensors and to optimize their performance for practical applications. The increase in pressure during the synthesis of CNFs can be considered as one of the ways to modify the sensing behavior of materials for NO₂ detection.

4. Conclusions

The obtained results showed the high potential of the CO_x-free method for the synthesis of carbon nanofibers for NO₂ detection at room temperature. Pristine CNF-based sensors demonstrated a response of 1.7% to 1 ppm NO₂. It was found that CNFs were more sensitive toward NO₂ compared to NH₃. The increase in the rate of CNF formation at 1 atm leads to the formation of strongly curved nanofibers, which is apparently shown using Raman spectroscopy by the highest I(D)/I(G) ratio. The CNFs with higher curvature degrees possessed higher concentrations of defects since these regions are under strain, and this explains the highest disorder degree and sensitivity of the sensor based on CNFs synthesized by methane decomposition at 1 atm. The modified Langmuir isotherm was more suitable for fitting the response data and showed the physical adsorption as dominating mechanism of interaction of nitrogen dioxide with the surface of CNFs. The investigated CNFs can be considered as suitable active materials for all-carbon gas sensors operating at room temperature. It was found that an increase in the pressure of the catalytic decomposition of methane led to a decrease in the response to NO₂. The sensor response was found to be enhanced by humidity for all CNFs, which is caused by the strong donation of protons from water molecules. The humidity-enhanced response was detected for CNFs synthesized at pressures higher than atmospheric pressure. This feature of CNFs could be a benefit for operating sensors in wet air or other gas mixtures with high humidity.

Supplementary Materials: The following supporting information can be downloaded at: <https://www.mdpi.com/article/10.3390/chemosensors11070381/s1>, Figure S1: SEM images of the CNFs on the substrate: CNFs-1 (a,b), CNFs-3 (c,d), CNFs-5 (e,f); Figure S2. The impact of concentration of NO₂ to response of CNF films (RH = 1%).

Author Contributions: Conceptualization, P.B.K., A.G.B. and N.I.L.; methodology, A.G.B., A.V.I., A.V.U., E.A.M. and D.S.K.; investigation, N.I.L., T.V.L., V.I.S., A.V.I., A.V.U., E.A.M., D.S.K., Y.A.C. and P.B.K.; writing—original draft preparation, A.G.B., N.I.L., P.B.K., T.V.L. and Y.A.C.; supervision, A.G.B. All authors have read and agreed to the published version of the manuscript.

Funding: The work was supported by the Russian Federation Ministry of Science and Higher Education (state research target, project no. FSUN-2023-0008).

Institutional Review Board Statement: Not applicable.

Informed Consent Statement: Not applicable.

Data Availability Statement: Not applicable.

Acknowledgments: The experiments were performed using facilities of the Shared Research Center “National Center of Investigation of Catalysts” at Boreskov Institute of Catalysis. The Raman spectra were registered using the equipment of the Center of Collective Usage “VTAN” in the ATRC department of Novosibirsk State University.

Conflicts of Interest: The authors declare no conflict of interest.

References

1. Pannullo, F.; Lee, D.; Neal, L.; Dalvi, M.; Agnew, P.; O'Connor, F.M.; Mukhopadhyay, S.; Sahu, S.; Sarran, C. Quantifying the impact of current and future concentrations of air pollutants on respiratory disease risk in England. *Environ. Health* **2017**, *16*, 29. [[CrossRef](#)]
2. Costa, S.; Ferreira, J.; Silveira, C.; Costa, C.; Lopes, D.; Relvas, H.; Borrego, C.; Roebeling, P.; Miranda, A.I.; Paulo Teixeira, J. Integrating health on air quality assessment—Review report on health risks of two major European outdoor air pollutants: PM and NO₂. *J. Toxicol. Environ. Health Part B* **2014**, *17*, 307–340. [[CrossRef](#)]
3. Zeng, W.; Zhao, H.; Liu, R.; Yan, W.; Qiu, Y.; Yang, F.; Shu, C.; Zhan, Y. Association between NO₂ cumulative exposure and influenza prevalence in mountainous regions: A case study from southwest China. *Environ. Res.* **2020**, *189*, 109926. [[CrossRef](#)]

4. Achakulwisut, P.; Brauer, M.; Hystad, P.; Anenberg, S.C. Global, national, and urban burdens of paediatric asthma incidence attributable to ambient NO₂ pollution: Estimates from global datasets. *Lancet Planet. Health* **2019**, *3*, e166–e178. [[CrossRef](#)] [[PubMed](#)]
5. Dalefield, R. Smoke and Other Inhaled Toxicants. In *Veterinary Toxicology for Australia and New Zealand*; Dalefield, R., Ed.; Elsevier: Oxford, UK, 2017; Chapter 20; pp. 361–372. ISBN 978-0-12-420227-6.
6. Virghileanu, M.; Săvulescu, I.; Mihai, B.-A.; Nistor, C.; Dobre, R. Nitrogen Dioxide (NO₂) Pollution Monitoring with Sentinel-5P Satellite Imagery over Europe during the Coronavirus Pandemic Outbreak. *Remote Sens.* **2020**, *12*, 3575. [[CrossRef](#)]
7. Lee, S.W.; Lee, W.; Hong, Y.; Lee, G.; Yoon, D.S. Recent advances in carbon material-based NO₂ gas sensors. *Sens. Actuators B Chem.* **2018**, *255*, 1788–1804. [[CrossRef](#)]
8. Kwak, D.; Lei, Y.; Maric, R. Ammonia gas sensors: A comprehensive review. *Talanta* **2019**, *204*, 713–730. [[CrossRef](#)]
9. Jeong, Y.; Hong, S.; Jung, G.; Shin, W.; Lee, C.; Park, J.; Kim, D.; Lee, J.-H. Effects of oxygen gas in the sputtering process of the WO₃ sensing layer on NO₂ sensing characteristics of the FET-type gas sensor. *Solid-State Electron.* **2023**, *200*, 108563. [[CrossRef](#)]
10. Inoue, T.; Ohtsuka, K.; Yoshida, Y.; Matsuura, Y.; Kajiyama, Y. Metal oxide semiconductor NO₂ sensor. *Sens. Actuators B Chem.* **1995**, *25*, 388–391. [[CrossRef](#)]
11. Liu, S.; Wang, Z.; Zhang, Y.; Zhang, C.; Zhang, T. High performance room temperature NO₂ sensors based on reduced graphene oxide-multiwalled carbon nanotubes-tin oxide nanoparticles hybrids. *Sens. Actuators B Chem.* **2015**, *211*, 318–324. [[CrossRef](#)]
12. Dinu, L.A.; Buiculescu, V.; Baracu, A.M. Recent Progress on Nanomaterials for NO₂ Surface Acoustic Wave Sensors. *Nanomaterials* **2022**, *12*, 2120. [[CrossRef](#)] [[PubMed](#)]
13. Li, M.; Kan, H.; Chen, S.; Feng, X.; Li, H.; Li, C.; Fu, C.; Quan, A.; Sun, H.; Luo, J.; et al. Colloidal quantum dot-based surface acoustic wave sensors for NO₂-sensing behavior. *Sens. Actuators B Chem.* **2019**, *287*, 241–249. [[CrossRef](#)]
14. Vanalakar, S.A.; Patil, V.L.; Harale, N.S.; Vhanalakar, S.A.; Gang, M.G.; Kim, J.Y.; Patil, P.S.; Kim, J.H. Controlled growth of ZnO nanorod arrays via wet chemical route for NO₂ gas sensor applications. *Sens. Actuators B Chem.* **2015**, *221*, 1195–1201. [[CrossRef](#)]
15. Navale, Y.H.; Navale, S.T.; Ramgir, N.S.; Stadler, F.J.; Gupta, S.K.; Aswal, D.K.; Patil, V.B. Zinc oxide hierarchical nanostructures as potential NO₂ sensors. *Sens. Actuators B Chem.* **2017**, *251*, 551–563. [[CrossRef](#)]
16. Mali, S.M.; Narwade, S.S.; Navale, Y.H.; Tayade, S.B.; Digraaskar, R.V.; Patil, V.B.; Kumbhar, A.S.; Sathe, B.R. Heterostructural CuO–ZnO Nanocomposites: A Highly Selective Chemical and Electrochemical NO₂ Sensor. *ACS Omega* **2019**, *4*, 20129–20141. [[CrossRef](#)]
17. Na, C.W.; Woo, H.-S.; Kim, I.-D.; Lee, J.-H. Selective detection of NO₂ and C₂H₅OH using a Co₃O₄-decorated ZnO nanowire network sensor. *Chem. Commun.* **2011**, *47*, 5148–5150. [[CrossRef](#)] [[PubMed](#)]
18. Yoo, Y.-S.; Bhardwaj, A.; Hong, J.-W.; Im, H.-N.; Song, S.-J. Sensing Performance of a YSZ-Based Electrochemical NO₂ Sensor Using Nanocomposite Electrodes. *J. Electrochem. Soc.* **2019**, *166*, B799. [[CrossRef](#)]
19. Shah, S.; Han, S.; Hussain, S.; Liu, G.; Shi, T.; Shaheen, A.; Xu, Z.; Wang, M.; Qiao, G. NO₂ gas sensing responses of In₂O₃ nanoparticles decorated on GO nanosheets. *Ceram. Int.* **2022**, *48*, 12291–12298. [[CrossRef](#)]
20. Barbosa, M.S.; Suman, P.H.; Kim, J.J.; Tuller, H.L.; Varela, J.A.; Orlandi, M.O. Gas sensor properties of Ag- and Pd-decorated SnO micro-disks to NO₂, H₂ and CO: Catalyst enhanced sensor response and selectivity. *Sens. Actuators B Chem.* **2017**, *239*, 253–261. [[CrossRef](#)]
21. Tang, T.; Li, Z.; Cheng, Y.F.; Xie, H.G.; Wang, X.X.; Chen, Y.L.; Cheng, L.; Liang, Y.; Hu, X.Y.; Hung, C.M.; et al. In-situ mechanochemically tailorable 2D gallium oxyselenide for enhanced optoelectronic NO₂ gas sensing at room temperature. *J. Hazard. Mater.* **2023**, *451*, 131184. [[CrossRef](#)]
22. Zhao, Q.; Zhou, W.; Zhang, M.; Wang, Y.; Duan, Z.; Tan, C.; Liu, B.; Ouyang, F.; Yuan, Z.; Tai, H.; et al. Edge-Enriched Mo₂TiC₂T_x/MoS₂ Heterostructure with Coupling Interface for Selective NO₂ Monitoring. *Adv. Funct. Mater.* **2022**, *32*, 2203528. [[CrossRef](#)]
23. Choi, J.; Kim, Y.-J.; Cho, S.-Y.; Park, K.; Kang, H.; Kim, S.J.; Jung, H.-T. In Situ Formation of Multiple Schottky Barriers in a Ti₃C₂ MXene Film and its Application in Highly Sensitive Gas Sensors. *Adv. Funct. Mater.* **2020**, *30*, 2003998. [[CrossRef](#)]
24. Yang, Z.; Zou, H.; Zhang, Y.; Liu, F.; Wang, J.; Lv, S.; Jiang, L.; Wang, C.; Yan, X.; Sun, P.; et al. The Introduction of Defects in Ti₃C₂T_x and Ti₃C₂T_x-Assisted Reduction of Graphene Oxide for Highly Selective Detection of ppb-Level NO₂. *Adv. Funct. Mater.* **2022**, *32*, 2108959. [[CrossRef](#)]
25. Nufer, S.; Lynch, P.J.; Large, M.J.; Ogilvie, S.P.; Salvage, J.P.; Pelaez-Fernandez, M.; Waters, T.; Jurewicz, I.; Muñoz, E.; Arenal, R.; et al. Laser-Deposited Carbon Aerogel Derived from Graphene Oxide Enables NO₂-Selective Parts-per-Billion Sensing. *ACS Appl. Mater. Interfaces* **2020**, *12*, 39541–39548. [[CrossRef](#)]
26. Zhang, Y.-H.; Wang, C.-N.; Yue, L.-J.; Chen, J.-L.; Gong, F.-L.; Fang, S.-M. Nitrogen-doped graphene quantum dot decorated ultra-thin ZnO nanosheets for NO₂ sensing at low temperatures. *Phys. E Low-Dimens. Syst. Nanostruct.* **2021**, *133*, 114807. [[CrossRef](#)]
27. Sysoev, V.I.; Yamaletdinov, R.D.; Plyusnin, P.E.; Okotrub, A.V.; Bulusheva, L.G. Adsorption kinetics of NO₂ gas on oxyfluorinated graphene film. *Phys. Chem. Chem. Phys.* **2023**, *25*, 2084–2089. [[CrossRef](#)]
28. Sacco, L.; Forel, S.; Florea, I.; Cojocaru, C.-S. Ultra-sensitive NO₂ gas sensors based on single-wall carbon nanotube field effect transistors: Monitoring from ppm to ppb level. *Carbon* **2020**, *157*, 631–639. [[CrossRef](#)]

29. Wang, X.; Wei, M.; Li, X.; Shao, S.; Ren, Y.; Xu, W.; Li, M.; Liu, W.; Liu, X.; Zhao, J. Large-Area Flexible Printed Thin-Film Transistors with Semiconducting Single-Walled Carbon Nanotubes for NO₂ Sensors. *ACS Appl. Mater. Interfaces* **2020**, *12*, 51797–51807. [[CrossRef](#)] [[PubMed](#)]
30. Sedelnikova, O.V.; Sysoev, V.I.; Gurova, O.A.; Ivanov, Y.P.; Koroteev, V.O.; Arenal, R.; Makarova, A.A.; Bulusheva, L.G.; Okotrub, A. V Role of interface interactions in the sensitivity of sulfur-modified single-walled carbon nanotubes for nitrogen dioxide gas sensing. *Carbon* **2022**, *186*, 539–549. [[CrossRef](#)]
31. Zhang, M.; Inoue, S.; Matsumura, Y. Light and flexible gas sensors made of free-standing carbon nanotube paper. *Chem. Phys. Lett.* **2020**, *747*, 137367. [[CrossRef](#)]
32. Karimi, E.Z.; Vahdati-Khaki, J.; Zebarjad, S.M.; Bataev, I.A.; Bannov, A.G. A novel method for fabrication of Fe catalyst used for the synthesis of carbon nanotubes. *Bull. Mater. Sci.* **2014**, *37*, 1031–1038. [[CrossRef](#)]
33. Sayago, I.; Santos, H.; Horrillo, M.C.; Alexandre, M.; Fernández, M.J.; Terrado, E.; Tacchini, I.; Aroz, R.; Maser, W.K.; Benito, A.M.; et al. Carbon nanotube networks as gas sensors for NO₂ detection. *Talanta* **2008**, *77*, 758–764. [[CrossRef](#)]
34. Bannov, A.G.; Lapekin, N.I.; Kurmashov, P.B.; Ukhina, A.V.; Manakhov, A. Room-Temperature NO₂ Gas Sensors Based on Granulated Carbon Nanofiber Material. *Chemosensors* **2022**, *10*, 525. [[CrossRef](#)]
35. Lee, J.S.; Kwon, O.S.; Shin, D.H.; Jang, J. WO₃ nanonodule-decorated hybrid carbon nanofibers for NO₂ gas sensor application. *J. Mater. Chem. A* **2013**, *1*, 9099–9106. [[CrossRef](#)]
36. Monereo, O.; Prades, J.D.; Cirera, A. Self-heating effects in large arrangements of randomly oriented carbon nanofibers: Application to gas sensors. *Sens. Actuators B Chem.* **2015**, *211*, 489–497. [[CrossRef](#)]
37. Monereo, O.; Casals, O.; Prades, J.D.; Cirera, A. Self-heating in pulsed mode for signal quality improvement: Application to carbon nanostructures-based sensors. *Sens. Actuators B Chem.* **2016**, *226*, 254–265. [[CrossRef](#)]
38. Kuvshinov, D.G.; Kurmashov, P.B.; Bannov, A.G.; Popov, M.V.; Kuvshinov, G.G. Synthesis of Ni-based catalysts by hexamethylenetetramine-nitrates solution combustion method for co-production of hydrogen and nanofibrous carbon from methane. *Int. J. Hydrog. Energy* **2019**, *44*, 16271–16286. [[CrossRef](#)]
39. Lumbers, B.; Barley, J.; Platte, F. Low-emission hydrogen production via the thermo-catalytic decomposition of methane for the decarbonisation of iron ore mines in Western Australia. *Int. J. Hydrog. Energy* **2022**, *47*, 16347–16361. [[CrossRef](#)]
40. Ermakova, M.A.; Ermakov, D.Y.Y.; Kuvshinov, G.G. Effective catalysts for direct cracking of methane to produce hydrogen and filamentous carbon. Part I. Nickel catalysts. *Appl. Catal. A Gen.* **2000**, *201*, 61–70. [[CrossRef](#)]
41. Xu, Y.; Zhang, C.; Zhou, M.; Fu, Q.; Zhao, C.; Wu, M.; Lei, Y. Highly nitrogen doped carbon nanofibers with superior rate capability and cyclability for potassium ion batteries. *Nat. Commun.* **2018**, *9*, 1720. [[CrossRef](#)]
42. De Volder, M.F.L.; Tawfick, S.H.; Baughman, R.H.; Hart, A.J. Carbon nanotubes: Present and future commercial applications. *Science* **2013**, *339*, 535–539. [[CrossRef](#)]
43. Lebrón-Colón, M.; Meador, M.A.; Lukco, D.; Solá, F.; Santos-Pérez, J.; McCorkle, L.S. Surface oxidation study of single wall carbon nanotubes. *Nanotechnology* **2011**, *22*, 455707. [[CrossRef](#)] [[PubMed](#)]
44. Kurmashov, P.B.; Bannov, A.G.; Popov, M.V.; Brester, A.E.; Ukhina, A.V.; Ishchenko, A.V.; Maksimovskii, E.A.; Tolstobrova, L.I.; Chulkov, A.O.; Kuvshinov, G.G. CO_x-free catalytic decomposition of methane over solution combustion synthesis derived catalyst: Synthesis of hydrogen and carbon nanofibers. *Int. J. Energy Res.* **2022**, *46*, 11957–11971. [[CrossRef](#)]
45. Zhu, Y.A.; Sui, Z.J.; Zhao, T.J.; Dai, Y.C.; Cheng, Z.M.; Yuan, W.K. Modeling of fishbone-type carbon nanofibers: A theoretical study. *Carbon* **2005**, *43*, 1694–1699. [[CrossRef](#)]
46. Kuvshinov, G.G.; Chukanov, I.S.; Krutsky, Y.L.; Ochkov, V.V.; Zaikovskii, V.I.; Kuvshinov, D.G. Changes in the properties of fibrous nanocarbons during high temperature heat treatment. *Carbon* **2009**, *47*, 215–225. [[CrossRef](#)]
47. Mazo, M.A.; Sanguino, J.; Martín-Gullón, I.; Rubio, J. Formation of carbon nanofibers with Ni catalyst supported on a micro-mesoporous glass. *Microporous Mesoporous Mater.* **2021**, *323*, 111168. [[CrossRef](#)]
48. Bannov, A.G.; Uvarov, N.F.; Ukhina, A.V.; Chukanov, I.S.; Dyukova, K.D.D.; Kuvshinov, G.G. Structural changes in carbon nanofibers induced by ball milling. *Carbon* **2012**, *50*, 1090–1098. [[CrossRef](#)]
49. Cao, A.; Xu, C.; Liang, J.; Wu, D.; Wei, B. X-ray diffraction characterization on the alignment degree of carbon nanotubes. *Chem. Phys. Lett.* **2001**, *344*, 13–17. [[CrossRef](#)]
50. Ferrari, A.C.; Robertson, J. Interpretation of Raman spectra of disordered and amorphous carbon. *Phys. Rev. B* **2000**, *61*, 14095. [[CrossRef](#)]
51. Jia, G.; Pan, F.; Bao, J.; Song, X.; Zhang, Y. Curvature effect of vacancies in single-walled carbon nanotubes. *Surf. Sci.* **2015**, *633*, 29–37. [[CrossRef](#)]
52. Bannov, A.G.A.G.; Jašek, O.; Manakhov, A.; Márik, M.; Nečas, D.; Zajíčková, L. High-performance ammonia gas sensors based on plasma treated carbon nanostructures. *IEEE Sens. J.* **2017**, *17*, 1964–1970. [[CrossRef](#)]
53. Ma, D.; Su, Y.; Tian, T.; Yin, H.; Huo, T.; Shao, F.; Yang, Z.; Hu, N.; Zhang, Y. Highly Sensitive Room-Temperature NO₂ Gas Sensors Based on Three-Dimensional Multiwalled Carbon Nanotube Networks on SiO₂ Nanospheres. *ACS Sustain. Chem. Eng.* **2020**, *8*, 13915–13923. [[CrossRef](#)]
54. Bannov, A.G.; Popov, M.V.; Brester, A.E.; Kurmashov, P.B. Recent Advances in Ammonia Gas Sensors Based on Carbon Nanomaterials. *Micromachines* **2021**, *12*, 186. [[CrossRef](#)]
55. Bannov, A.G.; Jašek, O.; Prášek, J.; Buršík, J.; Zajíčková, L. Enhanced ammonia adsorption on directly deposited nanofibrous carbon films. *J. Sens.* **2018**, *2018*, 7497619. [[CrossRef](#)]

56. Sharma, S.; Hussain, S.; Sengupta, K.; Islam, S.S. Development of MWCNTs/alumina composite-based sensor for trace level ammonia gas sensing. *Appl. Phys. A Mater. Sci. Process.* **2013**, *111*, 965–974. [[CrossRef](#)]
57. Kumar, S.; Pavelyev, V.; Mishra, P.; Tripathi, N. A review on chemiresistive gas sensors based on carbon nanotubes: Device and technology transformation. *Sens. Actuators A Phys.* **2018**, *283*, 174–186. [[CrossRef](#)]
58. Wu, D.; Peng, Q.; Wu, S.; Wang, G.; Deng, L.; Tai, H.; Wang, L.; Yang, Y.; Dong, L.; Zhao, Y.; et al. A simple graphene NH₃ gas sensor via laser direct writing. *Sensors* **2018**, *18*, 4405. [[CrossRef](#)]
59. Zhu, S.; Sun, H.; Liu, X.; Zhuang, J.; Zhao, L. Room-Temperature NH₃ sensing of graphene oxide film and its enhanced response on the laser-Textured silicon. *Sci. Rep.* **2017**, *7*, 14773. [[CrossRef](#)]
60. Bannov, A.G.; Prášek, J.; Jašek, O.; Shibaev, A.A.; Zajíčková, L. Investigation of Ammonia Gas Sensing Properties of Graphite Oxide. *Procedia Eng.* **2016**, *168*, 231–234. [[CrossRef](#)]
61. Srinivasreddy, R.K.; Kadeppagari, R.-K. Functionalized Carbon Nanotubes for Ammonia Sensors. In *Environmental Applications of Carbon Nanomaterials-Based Devices*; Wiley: Hoboken, NJ, USA, 2021; pp. 251–263. ISBN 9783527830978.
62. Panes-Ruiz, L.A.; Shaygan, M.; Fu, Y.; Liu, Y.; Khavrus, V.; Oswald, S.; Gemming, T.; Baraban, L.; Bezugly, V.; Cuniberti, G. Toward Highly Sensitive and Energy Efficient Ammonia Gas Detection with Modified Single-Walled Carbon Nanotubes at Room Temperature. *ACS Sens.* **2018**, *3*, 79–86. [[CrossRef](#)]
63. Kim, J.H.; Song, M.J.; Kim, K.B.; Jin, J.H.; Min, N.K. Evaluation of surface cleaning procedures in terms of gas sensing properties of spray-deposited CNT film: Thermal- and O₂ plasma treatments. *Sensors* **2017**, *17*, 73. [[CrossRef](#)] [[PubMed](#)]
64. Nguyen, L.Q.; Phan, P.Q.; Duong, H.N.; Nguyen, C.D.; Nguyen, L.H. Enhancement of NH₃ gas sensitivity at room temperature by carbon nanotube-based sensor coated with Co nanoparticles. *Sensors* **2013**, *13*, 1754–1762. [[CrossRef](#)]
65. Homagai, P.L.; Poudel, R.; Paudyal, H.; Ghimire, K.N.; Bhattarai, A. Adsorption of nitrate and nitrite anion by modified maize stalks from aqueous solutions. *Environ. Sci. Pollut. Res.* **2023**, *30*, 54682–54693. [[CrossRef](#)]
66. Mabuza, M.; Premllal, K.; Daramola, M.O. Modelling and thermodynamic properties of pure CO₂ and flue gas sorption data on South African coals using Langmuir, Freundlich, Temkin, and extended Langmuir isotherm models. *Int. J. Coal Sci. Technol.* **2022**, *9*, 45. [[CrossRef](#)]
67. Xiong, M.; Wang, B.; Wang, H.; Xu, F.; Zeng, Y.; Ren, H.; Zeng, H. Probing the adsorption behavior and mechanism of NO₂ and NH₂ functionalized covalent organic frameworks (COFs) for removal of bisphenol A. *Microporous Mesoporous Mater.* **2022**, *346*, 112299. [[CrossRef](#)]
68. Sohn, S.; Kim, D. Modification of Langmuir isotherm in solution systems—Definition and utilization of concentration dependent factor. *Chemosphere* **2005**, *58*, 115–123. [[CrossRef](#)]
69. Langmuir, I. The Adsorption of Gases on Plane Surfaces of Glass, Mica and Platinum. *J. Am. Chem. Soc.* **1918**, *40*, 1361–1403. [[CrossRef](#)]
70. Ju, L.; Tang, X.; Li, X.; Liu, B.; Qiao, X.; Wang, Z.; Yin, H. NO₂ Physical-to-Chemical Adsorption Transition on Janus WSSe Monolayers Realized by Defect Introduction. *Molecules* **2023**, *28*, 1644. [[CrossRef](#)] [[PubMed](#)]
71. Xu, Y.; Xie, J.; Zhang, Y.; Tian, F.H.; Yang, C.; Zheng, W.; Liu, X.; Zhang, J.; Pinna, N. Edge-enriched WS₂ nanosheets on carbon nanofibers boosts NO₂ detection at room temperature. *J. Hazard. Mater.* **2021**, *411*, 125120. [[CrossRef](#)] [[PubMed](#)]
72. Cha, J.-H.; Choi, S.-J.; Yu, S.; Kim, I.-D. 2D WS₂-edge functionalized multi-channel carbon nanofibers: Effect of WS₂ edge-abundant structure on room temperature NO₂ sensing. *J. Mater. Chem. A* **2017**, *5*, 8725–8732. [[CrossRef](#)]
73. Liou, W.-J.; Lin, H.-M. Nanohybrid TiO₂/carbon black sensor for NO₂ gas. *China Particuology* **2007**, *5*, 225–229. [[CrossRef](#)]
74. Kim, C.H.; Yoo, S.W.; Nam, D.W.; Seo, S.; Lee, J.H. Effect of temperature and humidity on NO₂ and NH₃ gas sensitivity of bottom-gate graphene FETs prepared by ICP-CVD. *IEEE Electron Device Lett.* **2012**, *33*, 1084–1086. [[CrossRef](#)]
75. Yan, W.; Worsley, M.A.; Pham, T.; Zettl, A.; Carraro, C.; Maboudian, R. Effects of ambient humidity and temperature on the NO₂ sensing characteristics of WS₂/graphene aerogel. *Appl. Surf. Sci.* **2018**, *450*, 372–379. [[CrossRef](#)]
76. Wang, X.; Chen, Y.; Qin, H.; Li, L.; Shi, C.; Liu, L.; Hu, J. CO₂ sensing of La_{0.875}Ca_{0.125}FeO₃ in wet vapor: A comparison of experimental results and first-principles calculations. *Phys. Chem. Chem. Phys.* **2015**, *17*, 13733–13742. [[CrossRef](#)]
77. Wang, Z.; Xiao, Y.; Cui, X.; Cheng, P.; Wang, B.; Gao, Y.; Li, X.; Yang, T.; Zhang, T.; Lu, G. Humidity-Sensing Properties of Urchinlike CuO Nanostructures Modified by Reduced Graphene Oxide. *ACS Appl. Mater. Interfaces* **2014**, *6*, 3888–3895. [[CrossRef](#)] [[PubMed](#)]
78. Bannov, A.G.; Jašek, O.; Manakhov, A.; Márik, M.; Nečas, D.; Zajíčková, L.; Prášek, J.; Jašek, O.; Zajíčková, L. Investigation of pristine graphite oxide as room-temperature chemiresistive ammonia gas sensing material. *Sensors* **2017**, *17*, 320. [[CrossRef](#)]
79. Tang, H.; Gao, C.; Yang, H.; Sacco, L.; Sokolovskij, R.; Zheng, H.; Ye, H.; Vollebregt, S.; Yu, H.; Fan, X.; et al. Room temperature ppt-level NO₂ gas sensor based on SnOx/Sn nanostructures with rich oxygen vacancies. *2D Mater.* **2021**, *8*, 45006. [[CrossRef](#)]
80. Park, J.-A.; Moon, J.; Lee, S.-J.; Kim, S.H.; Chu, H.Y.; Zyung, T. SnO₂-ZnO hybrid nanofibers-based highly sensitive nitrogen dioxides sensor. *Sens. Actuators B Chem.* **2010**, *145*, 592–595. [[CrossRef](#)]

Disclaimer/Publisher’s Note: The statements, opinions and data contained in all publications are solely those of the individual author(s) and contributor(s) and not of MDPI and/or the editor(s). MDPI and/or the editor(s) disclaim responsibility for any injury to people or property resulting from any ideas, methods, instructions or products referred to in the content.